Reusable nanocomposite membranes for highly efficient arsenite and arsenate dual removal from water

H. Salazar[1,2], P. M. Martins[",3,4], A. Valverde[5], R. Fernández de Luis[5], J. L. Vilas[5], S. Ferdov[1], G. Botelho[2], and S. Lanceros-Mendez[5,6]

[1]Centre/Department of Physics, [2]Centre/Department of Chemistry, [3]Centre of Molecular and Environmental Biology, University of Minho, Campus de Gualtar, 4710-057 Braga, Portugal

[4]IB-S – Institute for Research and Innovation on Bio-Sustainability, University of Minho, 4710-057, Braga, Portugal

[5]BCMaterials, Basque Center for Materials, Applications and Nanostructures, UPV/EHU Science Park, 48940 Leioa, Spain[6]IKERBASQUE, Basque Foundation for Science, 48009 Bilbao, Spain

Abstract

Nanocomposite membranes (NCMs) of poly (vinylidene fluoride-hexafluoropropylene), PVDF-HFP, with different loadings of yttrium carbonate and magnetite were prepared and their dual adsorption capacity over neutral arsenite and anionic arsenate species was evaluated. The NPs and the corresponding NCMs were fully characterised in terms of morphology, microstructure, thermal and surface properties. Nanocomposite membranes present a micrometric porous structure with a homogeneous distribution of the active nanoparticles. Chemical, thermal, and water-contact angle characteristics of the NCMs point out that they maintain the chemical and thermal stability of the polymer while improve wettability. Arsenic removal depends on NPs loading and pH of the media. For instance, efficiencies close to 100% were achieved for arsenate species under acidic conditions whilst adsorption capacity over arsenite was also incremented above 80%. Fe_3O_4/PVDF-HFP nanocomposite showed a dual affinity for the adsorption of As(III) and As(V) species, with maximum adsorption capacities of 92.82 and 137.08 mg/g, respectively. In addition, both NCMs are easily activated and reused without significant efficiency loss. Consequently, PVDF-HFP nanocomposites, especially the iron-based ones, represent a low-cost, reusable, and efficient water remediation systems suitable for the long-term removal of As(III) and As(V) under conditions mimicking real polluted surface and groundwater.

1. INTRODUCTION

Water quality is one of the biggest concerns nowadays, since climate change and rapid urbanization/industrialization lead to the overall pollution of the water cycle, and as a final consequence, to the decrease and depletion of potable water sources [1]. Heavy metals, [2] and specially negative oxyanions ((AsO_4^{3-}, CrO_4^{2-}, SeO_3^{2-}, etc. [3]) stand out as a systemic issues because of their intrinsic risks and their dual natural and anthropogenic origin.

Among these pollutants, the harmful effects of arsenate oxyanions are well-known in many geographical areas worldwide affected by arsenic pollution. Naturally, the main arsenic source is water lixiviation of arsenate anions from arsenic-rich minerals (e.g. arsenopyrite, mimetite, pyrite or adamite, among others) [4]. Anthropogenically, arsenic pollution is essentially associated with mining activity, arsenical pesticides, extensive exploitation of As-rich aquifers, and activities derived from coal-based thermal power plants [5]. As a consequence, it is estimated nowadays that more than 150 million people have been exposed to levels of As-contaminated water well above the legal limits in more than 70 countries [6]. Due to arsenic exposition, short and long-term effects have led to neurologic, respiratory, hepatic and reproductive health problems, its mutagenic capacity inducing also kidney, viscus and bladder cancers [7]. Consequently, World Health Organization (WHO) has defined a maximum concentration level for As in drinking water of 10 µg/L [8], being the mitigation of arsenic pollution an intense area of research nowadays [9].

In natural water sources, arsenic can be detected in both organic and inorganic forms and in different oxidation states (-3, 0, +3, +5), being more often present as As(III) and As(V) oxyanions with neutral and negative charges, respectively [10]. The predominance of each arsenic form is dependent of water properties, such as pH and oxidation/reduction potential, but in the most usual conditions found in surface and underground water, As(V) is found as negative oxyanions (i.e. $H_2AsO_4^-$, $HAsO_4^{2-}$, and AsO_4^{3-}) in oxidative conditions, whilst As(III) is stabilized as the neutral H_3AsO_3 form in water environments with low oxygen content [11].

Currently, different methods with varied degree of sophistication have been applied for As removal, including filtration [12], precipitation [13], ion-exchange [14], electrocoagulation [15], biological processes [16], membrane separation [17], and adsorption [18], among others. It is important to note that if the removal of As(V) negative species is challenging by itself, the

development of technical approaches to retain the As(III) neutral forms is even more difficult. Arsenite species lacks the electrical charge that usually promotes the adsorption or separation through electrostatics driven processes. Considering the pros and cons of current technologies, adsorption stands out as one of the most suitable, green and low cost alternatives due to its high efficiency, simple operation, the potential for re-utilisation and lack of side sludges generation [19]. Within this context, arsenic adsorption by iron and yttrium-based nanoparticles is one of the most promising approaches reported in the past few years to achieve a dual adsorption of arsenite and arsenate species [20, 21]. Moreover, some redox active metal oxides, especially iron-based nanomaterials, can work as As(III) to As(V) chemical oxidants too. However, recovering the nano-sorbents from the aqueous media after their use is not a minor issue since it usually implies the application of time and energy consuming procedures such as centrifugation or filtration [22].

The incorporation of dual nano-sorbents into mechanically robust polymeric matrices having the proper macro and meso porous structure is a suitable approach to overcome the previously mentioned drawbacks. In addition to the immobilization of the active nanomaterials, their overall adsorption efficiency is maintained within the polymeric matrix [23]. The straightforward strategy applied in this work opens the perspective to couple functionalities derived from the inorganic and organic nanocomponents but immobilized in a macroscopic membrane that can be easily handled, shaped, and reactivated for its prolonged application. For instance, the morphology, structure, and mechanical properties of the polymeric supports can be easily controlled through well-stablished protocols. The consequent combination of dual-adsorption within a membrane shaped polymeric technology fits the current technological needs to clean polluted waters derived from urban or industrial media. In this context, poly (vinylidene fluoride-co-hexafluoropropylene) (PVDF-HFP), is a chemical, thermal and mechanical robust polymer widely employed for water remediation purposes (i.e. removal or separation of organic and inorganic pollutants [24], organic matter [25], ions (desalination) [26], and heavy metals [27]). In addition, PVDF-HFP´s simple and well-studied processability opens the perspective to shape it as membrane with outstandingly tailorable porous structures [28]. Nonetheless, PVDF-HFP lacks the adsorption affinity to retain arsenic negative or neutral species. Here, the integration of metal-based nanotechnologies into porous PVDF matrixes comes into play to adsorb arsenic from relevant aqueous environments.

Herein, we have explored the synergistic combination of well-known arsenic nano-sorbents, such as Fe_3O_4 and $Y_2(CO_3)_3$ nanomaterials, with the filtration characteristics of PVDF membrane, which have resulted in a composite suitable for dual arsenate and arsenite water

remediation. Thus, the present work presents the development and evaluation of Fe_3O_4/PVDF-HFP and $Y_2(CO_3)_3$/PVDF-HFP composites as a technology to remove both As(V) and As(III) negative and neutral species from polluted waters. The nanocomposite membranes were characterized to understand their morphology and porous structure, assess their chemical, structural, and thermal properties, and correlate them with their As(III) and As(V) adsorption performance under different conditions. Adsorption kinetics, capacities, and reusability of metal-based/PVDF-HFP filters were studied under different conditions (i.e., pH, concentration) pointing out that the dual functionality of the metal-based nano-sorbents is maintained after their immobilization in PVDF-HFP macro and mesoporous matrixes.

2. MATERIALS AND METHODS

2.1. Materials

Poly (vinylidene fluoride-co-hexafluoropropylene) (PVDF-HFP), with a HFP content of 12 wt.% and a molecular weight of 600.000 g/mol, was obtained by Solvay. Magnetite (Fe_3O_4) nanoparticles were obtained from Nanostructured & Amorphous Materials, Inc. Yttrium carbonate ($Y_2(CO_3)_3$), N, N-dimethylformamide (DMF), sodium (meta)arsenite ($AsNaO_2$), sodium arsenate dibasic heptahydrate ($HAsNa_2O_4$), L-ascorbic acid, potassium antimony (III) tartrate hydrate, potassium permanganate, potassium phosphate dibasic, and hydrochloric acid were purchased from Sigma-Aldrich. Ammonium molybdate (VI) tetrahydrate was obtained from Acros Organics. Di-potassium hydrogen phosphate anhydrous was supplied from PanReac. Sodium hydroxide and sulfuric acid were purchased from VWR.

2.2. Nanocomposite membranes preparation

The nanocomposite membranes of Fe_3O_4/PVDF-HFP and Y/PVDF-HFP were prepared by solvent casting, as described in detail in [29]. Different amounts of Fe_3O_4 and $Y_2(CO_3)_3$ nanoparticles (NPs) were dispersed, under ultrasonication for 3 h in DMF to obtain composites with 3, 5, and 10 wt.% of metal-oxide nano-sorbents with respect to the PVDF-HFP matrix. After that, a certain amount of PVDF-HFP was added to the dispersion to achieve a PVDF-HFP/DMF concentration of 15:85 v/v. Then, the dispersion was magnetically stirred at 200 rpm until the polymer was completely dissolved. Finally, the solution was dropped into a Petri dish, and the solvent was evaporated at room temperature for $\approx$ 7 days.

2.3. Nanoparticle characterisation

X-ray diffraction (XRD) was applied to identify the crystalline phases of the iron and yttrium -based nanomaterials by using a Philips Analytical X-Ray PW1710 diffractometer (Cu Kα radiation (Kα_1=1.54056 Å and Kα_2 =1.54439 Å, Kα_{1/α_2} ratio= 0.5), 40 kV, 30 mA)), with a scanning range of 2θ = 10-80°, a step width of 0.02°, and time exposure of 10 seconds per point. Transmission Electron Microscopy (TEM) was performed with a TECNAI G2 20 TWIN apparatus operating at 200 kV and equipped with a LaB$_6$ filament. EDAX EDS microanalysis system and high angle annular dark-field-scanning transmission electron microscopy (HAADF-STEM) was carried out to identify the chemical composition of the nanocomposite membrane before and after their use. For TEM analysis, the samples were prepared by dispersion into ethanol and ultrasonication for 15 min. Finally, a drop of the suspension was spread onto a TEM copper grid (300 mesh) covered by a pure carbon film and dried under vacuum.

The Brunauer-Emmett-Teller (BET) method was used to determine the specific surface area of the nanomaterials. The nanomaterials were analysed at -176 °C by nitrogen adsorption-desorption in a Micromeritics TriStar analyser (Micromeritics). Before adsorption-desorption experiments, each sample was outgassed at 26.7 Pa and 350 °C for six hours.

The zeta (ζ) potential of the nanoparticles was performed by a Zetasizer NANO ZS-ZEN3600, Malvern (Malvern Instruments Limited, UK), equipped with a He–Ne laser (wavelength 633 nm) and backscatter detection (173°). Nanomaterials were dispersed in UP water and prepared at different pH values (3, 5, 7, 9 and 11) using 1M HCl and 1M NaOH solutions. The results were obtained using the Smoluchowski theory approximation, and each nanomaterial was measured ten times at 22 °C. The software (Zetasizer 7.12) was used to assess zeta potential values.

2.4. Nanocomposite membranes characterisation

The morphological characteristics of the Fe$_3$O$_4$/PVDF-HFP and Y/PVDF-HFP membranes was obtained by scanning electron microscopy (SEM), using a NanoSEM e FEI Nova 200 (FEG/SEM) with an accelerating voltage of 10 kV. The samples were previously coated with a 20 nm thick gold layer by sputtering with a Polaron SC502 apparatus.

Vibrational modes of the membranes were studied after Fourier Transformed Infrared Spectroscopy (FTIR) analysis, performed in the Attenuated Total Reflectance (ATR) mode at room temperature with a Jasco FT/IR-4100 apparatus. Measurements were conducted from 4000 to 600 cm^{-1} after 32 scans with a resolution of 4 cm^{-1}. Based on the absorbance observed

at 766 (α-PVDF) and 840 cm^{-1} (β-PVDF), the relative content of α and β phases of PVDF was calculated after equation 1, following the procedure described in [28].

$$F\,(\beta) = \frac{A_\beta}{(K_\beta/K_\alpha)A_\alpha + A_\beta} \quad (1)$$

where A_α and A_β are the absorbances at 766 and 840 cm^{-1} respectively, and K_α (6.1x10^4 cm^2/mol) and K_β (7.7x10^4 cm^2/mol) are the absorption coefficients at the corresponding wavenumber.

Difference Scanning Calorimetric (DSC) analyses were performed on Mettler-Toledo DSC 822e (Gießen, Germany) under heating-cooling-heating cycles from -100 to 200 °C, down to -100 °C and finally back up to 200 °C at a cooling rate of XXX. Measurements were carried out under N$_2$ atmosphere (flow rate 50mL/min) in aluminum pans with a sample mass of 7 to 10 mg. The degree of crystallinity (χ_c) of the NCMs was calculated according to equation 2:

$$\chi_c = \frac{\Delta H_f}{x\Delta H_\alpha + y\Delta H_\beta} \quad (2)$$

where ΔH_f is the melting enthalpy of the sample, x and y represent the α and β-phase contents of the sample, respectively, and ΔH_α and ΔH_β are the melting enthalpies for a 100% α-PVDF (93.04 J/g) and β-PVDF (104.40 J/g) crystalline samples, respectively.

The water contact angle of the samples was measured with an optical system Dataphysics OCA 15EC Neurtek Instrument. Drops of 2 μL volume of Milli-Q water were dropped on each sample. Triplicate measurements at different locations of each nanocomposite membrane were performed, averaging the contact angle values, calculated using the digital image.

### 2.5. Arsenic removal efficiency evaluation

Sodium arsenite and sodium arsenate were used as sources of As(III) and As(V) for the arsenic removal efficiency evaluation of the nanocomposite membranes. All the assays were performed in batch experiments. For that, a piece of the nanocomposite membrane with a defined mass (≈ 1 g) was placed in contact with 50 mL of an As solution. The solution was stirred for 6 hours, and aliquots were withdrawn at defined time intervals. Arsenic removal efficiency (E) and arsenic adsorption capacity (Q$_e$) were evaluated according to equations 3 and 4:

$$E\ (\%) = \frac{(C_i - C_f)}{C_i} \times 100 \quad (3)$$

$$Q_e = \frac{(C_i - C_f)V}{m} \quad (4)$$

where C_f and C_i are the final and initial arsenic concentration (mg/L), respectively, m is the mass (g) of adsorbent and V the volume (L) of the solution.

The experiments were performed with arsenic solutions with different pH values (4, 7 and 10), and As(III) and As(V) initial concentrations (1, 2, 5, 10, 25, and 50 mg/L). In order to quantify the As(III) and As(V) concentration during adsorption experiments, the arsenomolybdate (AsMo) colorimetry method was applied [30, 31]. The absorbance of the water samples after using the AsMo protocol were measured by UV-Vis spectrophotometry in a Tecan Infinite M Nano + spectrophotometer at 890 nm. After applying the protocol, the As(V) present in the solution was complexed to form an arsenomolybdate complex, according to the following equation:

$$12MoO_4^{2-} + AsO_4^{3-} + 24H^+ \rightarrow AsMo_{12}O_{40}^{3-} + 12H_2O \quad (5)$$
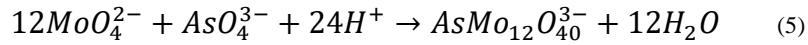
For As(III) quantification, a pre-oxidation step with a potassium permanganate solution was required. Afterwards, AsMo protocol was applied to quantify the arsenic concentration. Calibration curves for As(III) and As(V) were developed by applying the AsMo methodology to arsenic solutions of known concentrations between 0.01 to 10 mg/L.

2.6. Adsorption kinetics

Adsorption kinetics studies allow to understand the underpinning physical and chemical interactions governing the adsorption process. The rate of arsenic adsorption by NCMs was assessed in a batch experiment, as previously described. The NCMs were immersed within the arsenic solution under magnetic stirring for 6 hours. Aliquots were withdrawn at defined time intervals (0, 15, 30, 45, 60, 90, 120, 180, 240, and 360 min) to, later on, quantify the arsenic concentration. The kinetic curves were fitted according to nonlinear forms of pseudo-first, pseudo-second order, and Elovich models described in the equations 5, 6, and 7, respectively:

$$Q_t = Q_e\left(1 - exp^{(-k_1 t)}\right) \quad (5)$$

$$Q_t = \frac{Q_e^2 k_2 t}{1 + Q_e K_2 t} \quad (6)$$

$$Q_t = \frac{\ln \alpha\beta}{\beta} + \frac{1}{\beta} \ln t \quad (7)$$

where Q_e and Q_t (mg/g) are the capacities for arsenic adsorption at equilibrium and at a specific time, respectively. K_1 (min^{-1}) is the pseudo-first-order adsorption rate constant, K_2 (g·mg^{-1}·min^{-1}) is the pseudo second-order adsorption rate constant, α is the initial adsorption rate (mg·g^{-1}·min^{-1}) and β is the desorption constant (g·mg^{-1}).

2.7. Adsorption isotherms

Adsorption isotherms were obtained from batch experiments performed with As(III) and As(V) initial concentrations of 1, 2, 5, 10, 25, and 50 mg/L. A piece of NCMs of known weight ($\approx$ 1 g) are immersed in 50 mL of the arsenic solution under stirring for 6 hours. Afterwards, the final arsenic concentration was quantified, and the adsorption capacity in each point calculated considering the weight of the nanocomposite membrane. Adsorption isotherms are essential to evaluating the maximum adsorption capacity and the adsorption mechanisms of the studied nanocomposite materials. The isotherm curves were fitted to the following models: Langmuir, Freundlich, Temkin, Dubinin-Radushkevich, and Halsey, which are defined by the equations 7 to 12, respectively:

$$q_e = \frac{Q_{max} b C_e}{1 + b C_e} \quad (7)$$

$$q_e = K_F C_e^{1/n} \quad (8)$$

$$q_e = \frac{RT}{b_T} \ln(K_T C_e) \quad (9)$$

$$q_e = Q_S exp^{(-B_D \varepsilon^2)} \quad (10)$$

$$\varepsilon = RT \ln\left(1 + \frac{1}{C_e}\right) \quad (11)$$

$$q_e = K_H C_e^{1/n} \quad (12)$$

where q_e (mg/g) is the As adsorption capacity at a given equilibrium concentration, C_e (mg/L) is the arsenic equilibrium concentration, q_{max} (mg/g) is the maximum adsorption capacity, K_L (L/mg) is the adsorption rate for Langmuir isotherm model, K_F ($L^{1/n} \cdot mg^{(1-1/n)} \cdot g^{-1}$) is the adsorption capacity of the adsorbent for Freundlich isotherm model, and *1/n* is a measure of the adsorption intensity, *b* (J/mol) is the Temkin constant, K_T (L/g) is the Temkin isotherm constant, Q_S (mg/g) is the maximum adsorption capacity, B_D ($mol^2 \cdot kJ^{-2}$) is Dubinin-Radushkevich constant, ε (kJ/mol) is the adsorption potential, *R* (8.314 J/mol·K) is the universal gas constant, *T* (K) is the temperature, and K_H (L/g) and *n* are Halsey isotherm constants. Regarding to *1/n* value, the closer its value to 0, the more heterogeneous is the surface of the nanocomposite membrane.

3. RESULTS AND DISCUSSION

3.1. Nanomaterials characterisation

The morphology and microstructure of magnetite and yttrium carbonate (tengerite) NPs were studied by transmission electron microscopy (TEM) and X-ray diffraction (XRD (Figure 1 (a–c)). Fe_3O_4 NPs (Figure 1 a) present spherical and hexagonal shapes with particle diameters between 80 – 150 nm. $Y_2(CO_3)_3$ NPs (Figure 1 b) show a nanorod morphology, with sizes ranging from 50 to 200 nm diameter. The XRD pattern of Fe_3O_4 (Figure 1 c) shows the characteristic diffraction maxima of the simulated pattern obtained from the cubic spinel structure of magnetite [32, 33]. XRD pattern of yttrium carbonate (Figure 1 c) nanoparticles matches well with the simulated data obtained from the Y-Tengerite ($Y_2(CO_3)_{3.2} \cdot 3H_2O$) structural model [34-36].
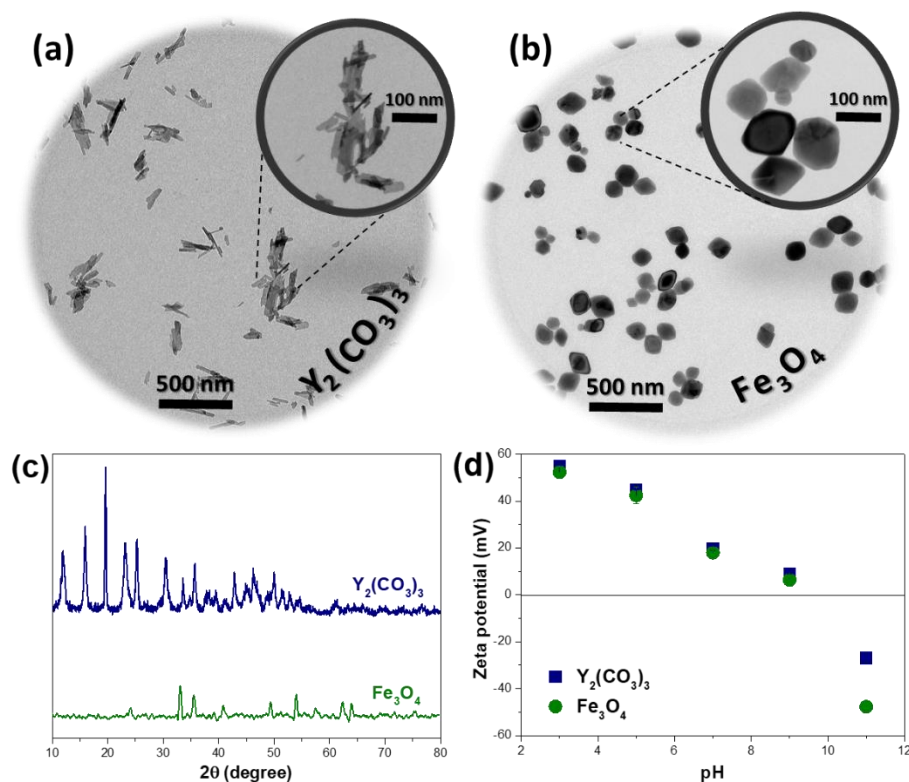
Figure 1. *TEM images of (a) Y₂(CO₃)₃ and (b) Fe₃O₄; (c) XRD patterns and (d) zeta potential of Y₂(CO₃)₃ and Fe₃O₄.*

The surface charge of the nanomaterials was quantified by zeta potential measurements (Figure 1 (d)). A similar surface charge dependence on the pH conditions is observed for both nanomaterials. The nanomaterials are positively charged under acidic and neutral environments, whereas at alkaline conditions, the surface charge becomes negative. Zero charge point (PZC) for both nano-sorbents is close to a pH value of 10.

3.2. Nanocomposite membrane characterisation

The morphology of the polymer matrixes and the dispersion of the nanoparticles in the nanocomposites were evaluated by the SEM images presented in Figure 2 for the PVDF-HFP, 10% Y/PVDF-HFP and 10% Fe_3O_4/PVDF-HFP samples.
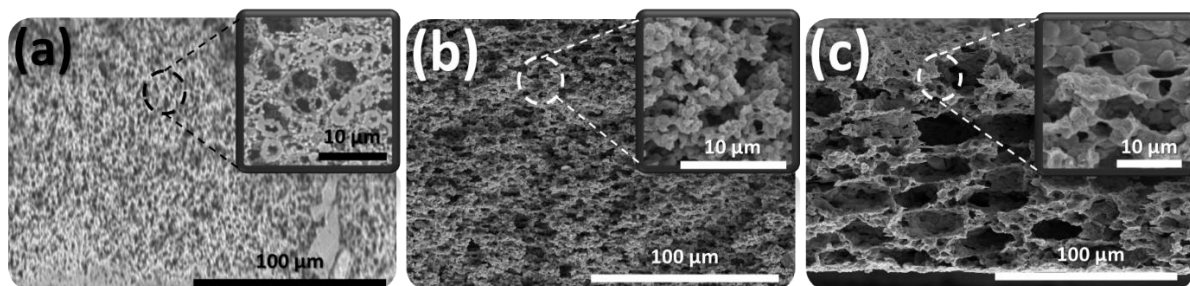

Figure 2. *SEM images of (a) PVDF-HFP, (b) 10% Y/PVDF-HFP, and (c) 10% Fe₃O₄/PVDF-HFP membranes.*

The slow evaporation of the solvent during sample preparation promotes a well-distributed and micrometric porous structure in the PVDF-HFP membrane, due to a liquid-liquid phase separation process (Figure 2 a-c) [37]. The pristine PVDF-HFP membranes exhibit a homogeneous spherulitic porous morphology. The inclusion of nanoparticles into the polymeric matrix does not affect significantly its morphology and structure (Figure 2 b and c) of the membranes. Nonetheless, a slight increase of the spherulitic size was observed for NCMs, more evident in the specific case of 10% Fe_3O_4/PVDF-HFP, which presents a combination of spheres and sponge-like structure. The latter is a typical structure of PVDF composite membranes with metal oxides [2].

The porous nature of 10% loaded PVDF nanocomposite membranes was quantified by BET measurements. 10% Fe_3O_4/PVDF-HFP membranes exhibit a 113 m^2/g surface area with inter and intraparticles porosities of 12 and 61 %, respectively. 10% Y/PVDF-HFP membranes show similar surface area (131 m^2/g), with inter and intraparticle porosities of 10 and 23%, respectively.

Table 1. <mark>BET measurements of Y/PVDF-HFP and Fe_3O_4/PVDF-HFP nanocomposite membranes.</mark>

	Total porosity (%)	Interparticle porosity (%)	Intraparticle porosity (%)	He density (g/cm³)	Theoretical porosity (%)	Surface area (m²/g)
Y/PVDF-HFP	73.88	12.03	61.85	1.89	73.89	113.8
Fe_3O_4/PVDF-HFP	33.69	10.45	23.24	1.68	33.69	131.5

The polymer characteristic crystalline phase and the thermal and wettability properties of the membranes were assessed by XRD, FTIR, DSC and contact angle measurements (Figure 3). X-ray diffraction patterns of 10% Fe_3O_4/PVDF-HFP and 10% Y/PVDF-HFP membranes confirm that the inclusion of the nanoparticles within the polymeric matrix does not affect their crystalline structure. Further, no additional peaks apart from those of PVDF, Fe_3O_4 and $Y_2(CO_3)_3$ are observed (Figure 3 a).
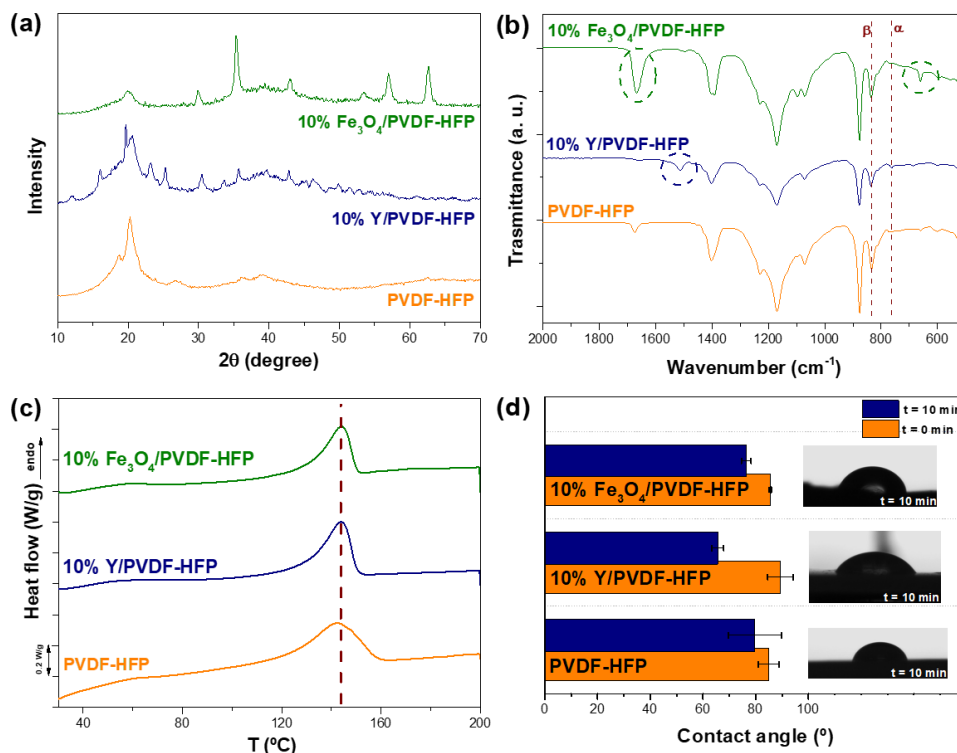
Figure 3. (a) XRD, (b) FTIR, (c) DSC, and (d) water contact angle measurements of the nanocomposite membranes.

The FTIR spectra of all the different samples show the characteristic bands of β-phase and α-phase PVDF at 838 and 760 cm^{-1}, respectively. In addition, the fingerprint adsorption bands of PVDF, C(F)–C(H)–C(F) skeletal bending, C–F_2 and C–C symmetrical stretching, and C–F stretching can be identified at 877, 1173, and 1400 cm^{-1}, respectively. As expected, the FTIR spectra of the NCMs present additional absorption bands related to the vibrational modes of the immobilized nanoparticles, such as the specific signal at 1514 cm^{-1}, characteristic of the C-O stretching vibration of carbonate groups[38], that can be found in the FTIR spectra of the 10% Y/PVDF-HFP membrane. The 10% Fe_3O_4/PVDF-HFP NCM exhibits two additional bands at 662 and 1664 cm^{-1}, related to the of Fe–O stretching vibration and OH–bending mode, respectively [39]. The β-phase content of PVDF-HFP (78%) is slightly increased when yttrium carbonate nanoparticles are used as filler. Nonetheless, it is noteworthy that all the membranes crystallise mainly as highly polar β-phase, which is related to the low solvent evaporation at room temperature [2].

The thermogram of the PVDF-HFP membrane (Figure 3 b) shows the characteristic endothermic peak (~140 ⁰C) attributed to the melting of the polymer crystalline phase [40]. The

12

incorporation of nanoparticles does not influences t the melting temperature of the polymeric matrix.

Water contact angle measurement for the PVDF-HFP membrane shows that its porous structure confers a hydrophilic nature to the surface regardless of the expected hydrophobicity of fluorinated compounds. Figure 3 (c) shows the water contact angle of the different membranes at an initial time and after 10 min with contact to a As standard solution. The pristine PVDF-HFP membrane present an initial contact angle of 85.0⁰, which after 10 min decreases to 79.7⁰. The incorporation of nanoparticles does not alter the wettability of the system. The hydrophilicity of PVDF-HFP/Fe and Y NCMs is a key feature in terms of membranes wettability and long-term membrane stability to remove chemical species from water.

3.3. Arsenic removal efficiency evaluation

An initial assessment of the NCMs adsorption kinetics and efficiency was performed in order to identify the effect of the nano-sorbents loading on their performance. After the identification of the best systems, the effect of the pH of the media on their adsorption kinetics was evaluated, later on, to unravel their kinetic and adsorption capabilities. Finally, acid activation protocols were applied to reactivate the nanocomposite membranes and assess their performance in five consecutive adsorption/desorption cycles.

3.3.1. Evaluation of the nanoparticles type and loading.

Kinetic curves for the different membranes were experimentally determined both for As(III) and As(V) solutions with an initial 5 mg/L concentration, an average value considering the arsenic levels found in polluted water sources worldwide [41, 42]. The results are presented in Figure 4, and the raw data have been summarised in Table S1.
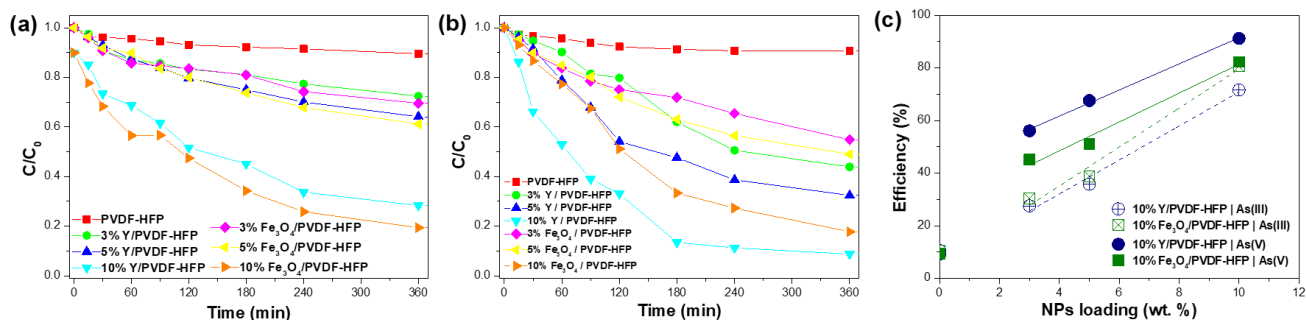
Figure 4. *Effect of Y and Fe₃O₄ nanoparticle content in polymer membrane on (a) As (III) and (b) As (V) removal; (c) dependence on the As(III) and As(V) adsoption efficiency over the nanoparticles loading within the polymeric nanocomposite membranes (pH = 7; [As] = 5 mg/L; contact time: 6 h).*

The PVDF-HFP membrane was tested as control. Efficiencies of 10.5 and 9.3% for As(III) and As(V) were obtained for the bare polymeric membrane, respectively. For NCMs, the higher the iron and yttrium nano-sorbents loading on the PVDF-HFP matrix, the faster and more effective the dual adsorption of arsenate and arsenite species. According to the final adsorption kinetic profiles represented in Figure 4 (a) and (b), iron-based nanocomposites show slightly higher efficiencies to remove As(III) than yttrium-based ones (80.6% *vs* 71.6%). This trend is also confirmed when comparing the adsorption capacities of both NCMs (2.45 mg/g *vs* 1.71 mg/g). On the contrary, 10% yttrium-based NCMs exhibit higher affinities and capacities to retain As(V) (91.2% and 2.90 mg/g) in comparison to 10% iron-based filters (82.3% and 2.66 mg/g). Figure 4 (c) summarizes the adsorption efficiency dependence on the nano-sorbents loading in the composite membranes. There is a linear increase of the arsenic removal (%) with the wt. (%) of iron and yttrium nanoparticles immobilized within the PVDF-HFP matrix. The slope of the linear trend observed in Figure 4 (c) suggests that a further increase of the NPs weight loading on the PVDF-HFP matrix would give rise to an As(III) adsorption efficiency over performance in comparison to As(V). Nevertheless, the higher the loading degree, the lower the mechanical strength of the nanocomposite membranes [43]. Considering the conclusions drawn by the adsorption kinetics, further adsorption studies were performed using the 10% Fe₃O₄/PVDF-HFP and 10% Y/PVDF-HFP NCMs.

3.3.2. *Adsorption dependence on the As(III) and As(V) speciation*

Arsenic speciation is highly dependent on redox and pH (Figure S1). According to *Moreira, V. R. et al* [17], under acidic and neutral pH values, anionic and neutral species are predominant both for As^{3+} ($H_2AsO_3^-$; H_3AsO_3) and As^{5+} ($H_2AsO_4^-$; $HAsO_4^{2-}$). Under alkaline conditions, the most predominant As (III) species are $HAsO_3^{2-}$ and $H_2AsO_3^-$, and the As (V) predominant forms

are $HAsO_4^{2-}$ and H_3AsO_4. Considering these factors, adsorption kinetic experiments were performed at three different pH values: 4, 7 and 10. Therefore, by exploring the adsorption efficiency of the developed system at the selected pH values, we are correlating the performance of the NCMs under the most usual conditions found in polluted water sources with their adsorption dependence as a function of the As(III) and As(V) species. The As(III) and As(V) kinetic curves at these conditions are shown in Figure 5, whilst the raw data have been summarized in Table S2.
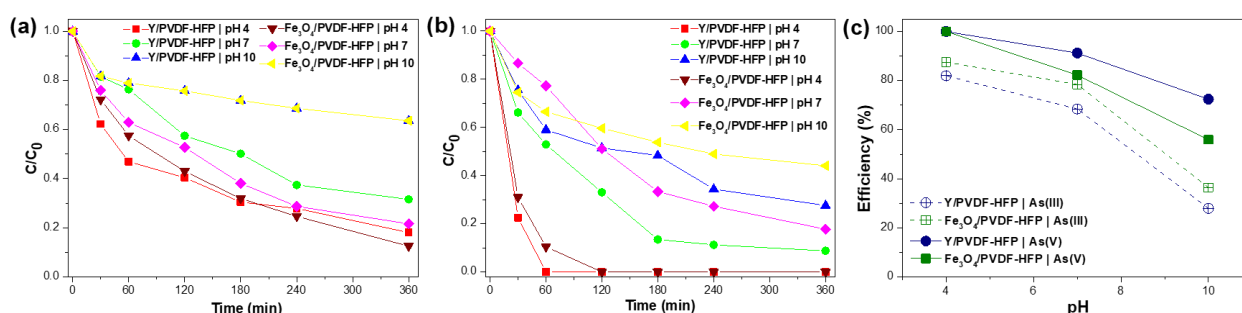

Figure 5. Effect of pH on (a) As (III) and (b) As (V) removal by NCMs; (c) pH dependence of the adsorption efficiency ([As] = 5 mg/L; contact time: 6 h).

As shown in Figure 5, both As(III) and As(V) removal is strongly dependent on the pH value. The most favourable conditions for the dual As(III) and As(V) adsorption are the acidic ones (pH 4). The adsorption efficiency of the NCMs decreases significantly at neutral or basic conditions, being more accused the performance loss and kinetics slow down for the specific case of As(V) anion. Thus, the overall adsorption efficiency and kinetics for As(III) and As(V) capture seem to be mainly governed by the surface charge of the nano-sorbents, and secondarily, by the arsenic speciation in the media. For instance, surface charge and functional groups of NPs are greatly affected by the pH of the environment, as demonstrated by their surface zeta potential [44]. As both Fe and Y based NPs are positively charged at acidic conditions, they welcome the adsorption of As(V) oxyanions through electrostatic interactions. However, as long as the pH value increases, the positive charge density decreases above ZPC, Fe_3O_4 and Y becoming negatively charged on their surface for pH values around XX. Electrostatic interaction between the NPs and arsenic species can be understood as the main factor governing the adsorption process for negatively charged As forms, but not the unique one since it cannot completely explain the adsorption of As(III) neutral species at acidic and neutral conditions, as well as the uptake of negative arsenate anion at the same conditions [17]. Under these considerations, alternative adsorption mechanisms need to be taken into account

to explain these findings, such as arsenite covalent chemisorption at the Y and Fe-based NPs' surface, or the anionic exchange of surface coordinatively bonded hydroxyl or carbonate groups.

3.3.3. Adsorption kinetics

The effect of the contact time between an adsorbent and a pollutant on the pollutant uptake efficiency is an essential factor to assess the technical feasibility of a developed technology. Adsorption kinetics is essential to quantify the behaviour of the adsorption process over time. Based on the data in Figure 6, most of the As(V) capture takes place during the first 3 hours of contact with the NCMs. As(III) adsorption is slower and occurs mostly in the first 4 hours. With those data, pseudo-first order, pseudo-second order, and Elovich kinetic models were used to fit the experimental results. Figure 6 shows the fitting for the pseudo-second order model whilst Figure S2 and Table S3 provide the adsorption kinetics simulation for As (III) and As (V) by applying all different models. Table S3 also summarizes the correlation coefficient (R^2), root-mean-square error (RMSE), and the adsorption rate constants (k, α) for each of the fittings.
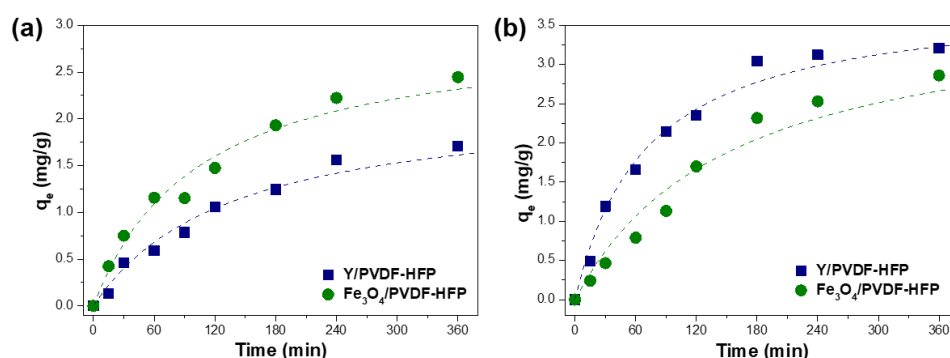

Figure 6. *Pseudo-second order adsorption kinetics of the nanocomposite membranes for (a) As (III) and (b) As (V) removal ([As] = 5 mg/L; contact time: 6 h; pH = 7).*

Based on the correlation coefficients, the kinetics data fit well with both pseudo-first and pseudo-second order models. The pseudo-second order model present smaller values of RMSE for almost all the nanocomposite membranes studies at different pH conditions. As pseudo-second-order model describes the adsorption as a chemical process, being reasonable to consider chemisorption an essential driving force of PVDF composites to capture arsenic [45]. As the RMSE values for pseudo-first and pseudo-second order models are similar, arsenic uptake by the composite filters can be explained as a combination of electrostatic and chemisorption processes.

3.3.4. Adsorption isotherms

The arsenic removal capacity of the NCMs was evaluated by determining and fitting the As(III) and As(V) adsorption isotherms to different models, xx, xxx, xx, xxx (Table S4). The fitting of the experimental isotherms to the Langmuir model is represented in Figure 7 and the parameters obtained from the fitting are summarized in Table S5. R^2 and RMSE were used to estimate the fit-quality of each model. For both As(III) and As(V) removal, Langmuir, Freundlich, and Halsey models present R^2 close to 1, indicating the suitability of the simulations for both NCMs [46]. Comparing the RMSE values, the Langmuir model shows the smallest value, and it is thus considered the most suitable one to predict arsenic adsorption. Based on the Langmuir fittings, the maximum adsorption capacities (Q_{max}) obtained for As(III) were 72.23 and 92.82 mg/g for Y/PVDF-HFP and Fe_3O_4/PVDF-HFP, respectively. For As(V), the obtained Q_{max} were 80.13 and 137.08 mg/g for Y/PVDF-HFP and Fe_3O_4/PVDF-HFP, respectively.
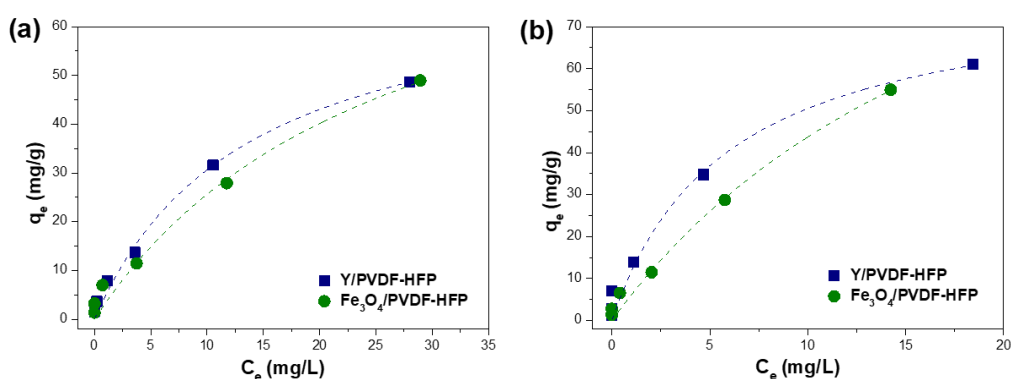

Figure 7. (a) As(III) and **(b)** As(V) adsorption Langmuir isotherm for nanocomposite membranes (contact time: 6 h; pH = 7).

The Langmuir model assumes that adsorption of arsenic takes place on a homogeneous surface and that all active sites have a similar affinity for As, which leads to the formation of a monolayer on the NCMs surface. In agreement with the conclusions drawn by the kinetics experiments, Langmuir fittings point out that arsenic removal occurs through a chemisorption process [47]. Chemisorption mechanisms have also been reported in works using yttrium [48] and iron oxide [49] nanoparticles as arsenic adsorbent.

Intensive efforts have been made to found novel solutions to remove both As(V) and As(III) from polluted water sources. Almost all researcher efforts focus on the use NPs´ suspensions to this end. In particular, metal-based nanomaterials have been extensively applied to capture arsenic species. *Lu, J. et al* [50] achieved a Q_{max} of 134.6 mg/g for As(V) removal with FeMn

bimetal oxides. However, the arsenic removal experiments were performed under extremely acidic pH. A work of *Zeng, H. et al* [51] reported a Q_{max} of 26.1 mg/g using maghemite (γ-Fe_2O_3) for consecutive uses, under acidic pH values (pH = 4). A Fe-Y binary oxide was used for the removal of As(V) in water at acidic pH, achieving a Q_{max} of 303 mg/g [52]. However, the high value of the adsorption capacities of these materials, the acidic environments and the use of these adsorbents in suspension are the main drawbacks of previous studies, preventing actual applications. Up to date, research on arsenic removal from water by polymers composite membranes has not been extensively reported since membrane separation is applied as a secondary treatment. *Yu, Y. et al* developed a Y/PVA modified PSF membrane for As(V) removal, achieving a Q_{max} of 35.56 mg/g. However, the adsorption experiments were performed far from the usual conditions found in water polluted sources [48]. *Liu, B. et al* applied α-Fe_3O_4 impregnated chitosan beads for As(III) removal. The system is reusable and exhibits a moderate Q_{max} of 6.18 mg/g after 6 h at pH 5 [53]. Compared to previous findings, the NCMs developed in this work show better performance in terms of adsorption capacities and kinetics, proven long-term reusability, and the dual adsorption functionality to capture both As(III) and As(V) species in a broad range of pH conditions. It is important to note that most of the studies deployed in this work have been performed under arsenic concentration and pH conditions relevant for arsenic pollutions sources found in many locations worldwide, such as Ghana ([As] = 4.5 mg/L, pH = 6) [54], Vietnam ([As] = 3.1 mg/L, pH = 6 – 8) [55], or Italy ([As] = 25 mg/L, pH $\approx$ 7) [56].

3.3.5. Recyclability of the membranes

To evaluate the reusability of the NCMs, the membranes were activated under magnetic stirring, during 4 h in a 1M NaOH solution, and afterwards, during 2 h hours by ultrapure water. After the desorption process, a new As solution was placed in contact with the NCMs to evaluate their performance. Five consecutive adsorption and desorption uses were carried out. The results of the reusability of the NCMs are presented in Figure 8, whilst the final adsorption efficiencies and capacities are summarized in Tables S6 and S7, and Figure S3.
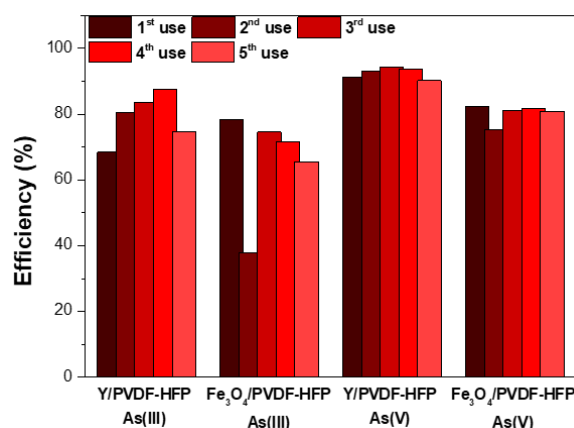
Figure 8. Recyclability of the nanocomposite membranes ([As] = 5 mg/L; contact time: 6 h; pH = 7).

As shown in Figure 8, Figure S3, and Tables S6 and S7, there are no significant efficiency losses after the reactivation of the NCMs, nor for As(III), neither for As(V). On the one hand, after the 5th cycle, a maximum efficiency loss of 12.8% was found for the removal of As(III) by the Fe_3O_4/PVDF-HFP nanocomposite membrane. On the other hand, Y/PVDF-HFP shows an efficiency enhancement of 6.3% for As(III) removal upon activation and reutilization of the composite. In general, the removal efficiencies remain constant, and therefore, the activation process seems to be effective in order to desorb all the arsenic present on active nanomaterials. These results point out that the NCMs are suitable for the treatment of As contaminated waters, and present potential to be applied on continuous treatment processes for this specific pollutant.

3.3.6. Adsorption mechanism

FTIR spectroscopy, SEM-EDX and XRD were used to gain insights into the adsorption mechanisms of Fe_3O_4 and Y nanocomposites over arsenic. Figure 9 presents the FTIR, XRD, and EDX elemental mapping of 10% Y and Fe_3O_4 based nanocomposite membranes before and after the adsorption of As(III) and As(V). EDX spectra of the NCMs before and after adsorption is presented in Figure S4.
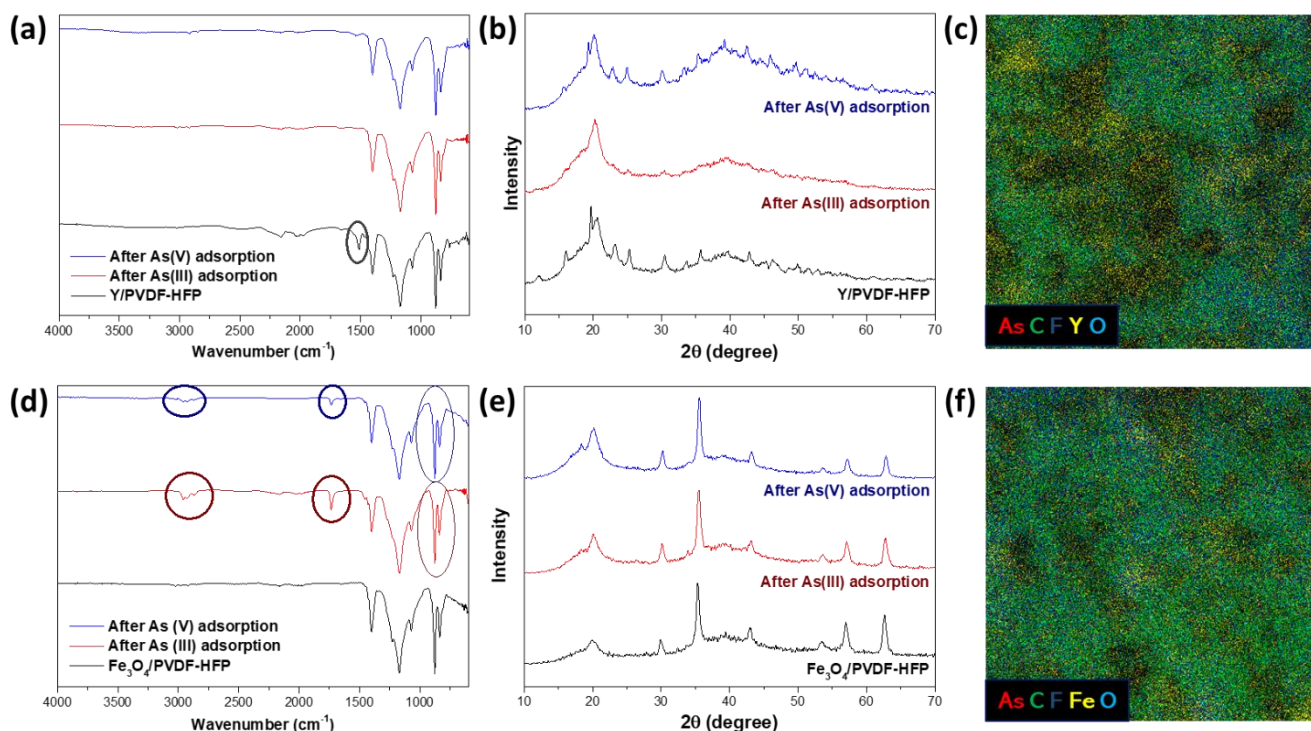
Figure 9. (a) FTIR spectra, (b) EDX micrograph, and (c) elemental mapping of Y/PVDF-HFP; (d) FTIR spectra, (e) EDX micrograph, and (f) elemental mapping of Fe₂O₃/PVDF-HFP.

The comparison of the FTIR spectra of the Y/PVDF-HFP membranes before and after arsenic adsorption reveal a significant decrease of the absorption band (≈ 1520 cm^{-1}) related to the stretching υ C=O vibrational mode of CO_3^{2-} groups. This experimental observation suggests that a partial replacement of carbonate by arsenate is occurring during the adsorption [57, 58]. In addition, an increase of intensity of the absorption band located at ≈ 835 cm^{-1}, associated with the vibrational modes of monodentate Y–O–As inner-sphere complex bonding, was also observed [59, 60]. X-ray diffraction patterns show that the intensity of the diffraction peaks related to the yttrium carbonate phase is reduced after the adsorption of As(III) and As(V) species. Indeed, the crystallinity loss of the $Y_2(CO_3)_3$ phase is accentuated in the case of As(III) in comparison to As(V). It is hypothesised that As(III) adsorption is driven by a two-step process, it starts with the oxidation of As(III) to As(V), and later on, the anion exchange per carbonate anions occurs. In addition, it is well known that anion exchange processes in solid ordered crystalline materials can give rise to the disruption of the long-range ordering, and as a consequence, to the amorphization of the parent phase. Further, the partial dissolution of yttrium carbonate phase can also explain the tendency observed by XRD, as it is not observed residual yttrium anions in the arsenic solutions after the adsorption process (Figure S4 a). EDX micrographs and elemental mapping presented in Figure 9 (c) and Figure S4 (a) confirmed the

presence of As on the membrane surface. For instance, arsenic is detected close to Y in the membrane, confirming that arsenic adsorption is mainly driven by the active nanoparticles incorporated within the polymeric PVDF-HFP matrix.

$$\equiv Y - CO_3^{2-} + As\,(V) \;\rightarrow\; Y - As\,(V) + CO_3^{2-} \quad (9)$$
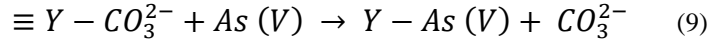
Comparing the spectra of Fe$_3$O$_4$/PVDF-HFP before and after adsorption of arsenic (Figure 9 d), several meaningful differences attributed to the arsenic coordination to magnetite nanoparticles are found. First, an increase of intensity was observed at $\approx$ 835 and $\approx$ 875 cm^{-1} due to the As–O–Fe stretching vibration. Second, the complexation of Fe–OH with arsenic [61, 62] gives rises to the appearance of an adsorption peak at $\approx$ 1735 cm^{-1}. Finally, the two bands appearing at $\approx$ 2930 and $\approx$ 2960 cm^{-1} further confirm the presence of As-O moieties in the composite polymers after arsenic adsorption [63]. Arsenic uptake by magnetite-based filters can be summarized as described in equation 10 [64].

$$\equiv Fe - OH + As\,(V) \; + \; H^+ \;\rightarrow\; Fe - As\,(V) + H_2O \quad (10)$$
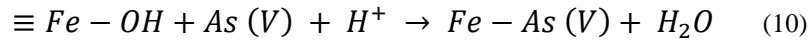
Contrary to yttrium carbonate, XRD patterns point that magnetite remains stable after the arsenic chemisorption. As observed in Figure 9 (f) and Figure S4 (b), EDX micrograph confirmed that arsenic was adsorbed on the NCM surface and the element mapping clearly exhibited the presence of iron and arsenic. Indeed, arsenic is located close to these areas where iron is detected, pointing that magnetite nanoparticles are the binding point for As(III) and As(V) based species. In line with the hypothesis for yttrium carbonate NCMs, magnetite seems to work as an As(III) to As(V) oxidant and absorber. The main difference is that the fixation of arsenic is likely to happen at the surface of the Fe$_3$O$_4$ nanoparticles instead of being controlled by an anion exchange process.

4. CONCLUSIONS

Nanocomposite membranes based on Y/PVDF-HFP and Fe$_3$O$_4$/PVDF-HFP with different amounts of Y$_2$(CO$_3$)$_3$ and Fe$_3$O$_4$ were prepared , characterised, and their adsorption removal efficiency over As(III) and As(V) evaluated. The NCMs presented a micrometric porous structure and a homogeneous distribution of the iron and yttrium based nanofillers. The incorporation of NPs does not affect the morphology, structure, thermal and wettability properties of membranes. The NPs loading on membrane matrix has a critical influence on their

As adsorption efficiency. For NCMs with 10% of NPs, a maximum absorption efficiency of 91.2% was achieved for the xxx membrane. The pH plays an essential role in the adsorption efficiency since it influences the surface charge of the NPs and arsenic speciation in solution. At acidic pH, the NCMs achieved an efficiency of 100.0%. Adsorption kinetics by the NCMs followed a pseudo-second-order kinetic model, which indicates that a chemical adsorption process occurs. The Langmuir isotherm model confirms chemisorption as the predominant arsenic uptake mechanism. Maximum adsorption capacities of 92.82 mg/g for As(III) and 137.08 mg/g for As(V) removal were achieved with Fe_3O_4/PVDF-HFP nanocomposite membrane. In addition, these NCMs present remarkable adsorption reusability, without significant loss of efficiency after 5 consecutive uses. In short, the prepared nanocomposite membranes proved to be suitable for the long-term removal from contaminated water of the most common and toxic forms of arsenic (As^{3+} and As^{5+}) in a wide range of concentrations and natural conditions .

References

1. Pei, X., et al., *Robust cellulose-based composite adsorption membrane for heavy metal removal.* Journal of Hazardous Materials, 2021. **406**.
2. Salazar, H., et al., *Poly(vinylidene fluoride-hexafluoropropylene)/bayerite composite membranes for efficient arsenic removal from water.* Materials Chemistry and Physics, 2016. **183**: p. 430-438.
3. Ghiorghita, C.A. and M. Mihai, *Recent developments in layer-by-layer assembled systems application in water purification.* Chemosphere, 2021. **270**.
4. Alka, S., et al., *Arsenic removal technologies and future trends: A mini review.* Journal of Cleaner Production, 2021. **278**: p. 123805.
5. Boussouga, Y.A., H. Frey, and A.I. Schäfer, *Removal of arsenic(V) by nanofiltration: Impact of water salinity, pH and organic matter.* Journal of Membrane Science, 2021. **618**.
6. Luan, H., B. Teychene, and H. Huang, *Efficient removal of As(III) by Cu nanoparticles intercalated in carbon nanotube membranes for drinking water treatment.* Chemical Engineering Journal, 2019. **355**: p. 341-350.

7.   Qiu, Z., et al., *Efficient oxidation and absorption of As(III) from aqueous solutions for environmental remediation via CuO@MNW membranes.* Separation and Purification Technology, 2020. **250**.

8.   Qiu, Z., et al., *Enhanced As(Ш) removal from aqueous solutions by recyclable Cu@MNM composite membranes via synergistic oxidation and absorption.* Water Research, 2020. **168**: p. 115147.

9.   Alka, S., et al., *Arsenic removal technologies and future trends: A mini review.* Journal of Cleaner Production, 2021. **278**.

10.   Yamaguchi, N., et al., *Arsenic Distribution and Speciation near Rice Roots Influenced by Iron Plaques and Redox Conditions of the Soil Matrix.* Environmental Science & Technology, 2014. **48**(3): p. 1549-1556.

11.   Wu, C., et al., *Oxic and anoxic conditions affect arsenic (As) accumulation and arsenite transporter expression in rice.* Chemosphere, 2017. **168**: p. 969-975.

12.   Bahmani, P., et al., *Arsenate removal from aqueous solutions using micellar-enhanced ultrafiltration.* Journal of Environmental Health Science and Engineering, 2019. **17**(1): p. 115-127.

13.   Vega-Hernandez, S., J. Weijma, and C.J.N. Buisman, *Immobilization of arsenic as scorodite by a thermoacidophilic mixed culture via As(III)-catalyzed oxidation with activated carbon.* J Hazard Mater, 2019. **368**: p. 221-227.

14.   Ortega, A., et al., *Arsenic removal from water by hybrid electro-regenerated anion exchange resin/electrodialysis process.* Separation and Purification Technology, 2017. **184**: p. 319-326.

15.   Sandoval, M.A., et al., *Arsenic and fluoride removal by electrocoagulation process: A general review.* Science of The Total Environment, 2021. **753**: p. 142108.

16.   Yan, H., et al., *Potential use of the Pteris vittata arsenic hyperaccumulation-regulation network for phytoremediation.* Journal of Hazardous Materials, 2019. **368**: p. 386-396.

17.   Moreira, V.R., et al., *Arsenic contamination, effects and remediation techniques: A special look onto membrane separation processes.* Process Safety and Environmental Protection, 2021. **148**: p. 604-623.

18.   Najib, N. and C. Christodoulatos, *Removal of arsenic using functionalized cellulose nanofibrils from aqueous solutions.* Journal of Hazardous Materials, 2019. **367**: p. 256-266.

19.   Asere, T.G., C.V. Stevens, and G. Du Laing, *Use of (modified) natural adsorbents for arsenic remediation: A review.* Science of The Total Environment, 2019. **676**: p. 706-720.

20.   Latif, A., et al., *Remediation of heavy metals polluted environment using Fe-based nanoparticles: Mechanisms, influencing factors, and environmental implications.* Environmental Pollution, 2020. **264**.

21.   Zhang, Y., et al., *Improved hydrogen storage performances of Mg-Y-Ni-Cu alloys by melt spinning.* Renewable Energy, 2019: p. 263-271.

22.   Salazar, H., et al., *Photocatalytic and antimicrobial multifunctional nanocomposite membranes for emerging pollutants water treatment applications.* Chemosphere, 2020. **250**.

23.   Martins, P.M., et al., *Comparative efficiency of TiO2 nanoparticles in suspension vs. immobilization into P(VDF–TrFE) porous membranes.* RSC Advances, 2016. **6**(15): p. 12708-12716.

24.   da Silva, R.J., et al., *Kinetics and thermodynamic studies of Methyl Orange removal by polyvinylidene fluoride-PEDOT mats.* Journal of Environmental Sciences (China), 2021. **100**: p. 62-73.

25.   Zhao, S., et al., *An antifouling catechol/chitosan-modified polyvinylidene fluoride membrane for sustainable oil-in-water emulsions separation.* Frontiers of Environmental Science and Engineering, 2021. **15**(4).

26.   Zuo, X., et al., *Desalination of water with a high degree of mineralization using SiO2/PVDF membranes.* Desalination, 2013. **311**: p. 150-155.

27.   Yao, Y., et al., *Zn-MoS2 nanocatalysts anchored in porous membrane for accelerated catalytic conversion of water contaminants.* Chemical Engineering Journal, 2020. **398**.

28.   Martins, P., A.C. Lopes, and S. Lanceros-Mendez, *Electroactive phases of poly(vinylidene fluoride): Determination, processing and applications.* Progress in Polymer Science, 2014. **39**(4): p. 683-706.

29.   Salazar, H., et al., *Poly(vinylidene fluoride-trifluoroethylene)/NAY zeolite hybrid membranes as a drug release platform applied to ibuprofen release.* Colloids and Surfaces A: Physicochemical and Engineering Aspects, 2015. **469**: p. 93-99.

30.   Rao, C.S.S., S.C.S. Rajan, and N.V. Rao, *Spectrophotometric determination of arsenic by molybdenum blue method in zinc-lead concentrates and related smelter products after chloroform extraction of iodide complex.* Talanta, 1993. **40**(5): p. 653-656.

31.   Lenoble, V., et al., *Arsenite oxidation and arsenate determination by the molybdene blue method.* Talanta, 2003. **61**(3): p. 267-276.

32.   Balbuena, J., et al., *Hematite porous architectures as enhanced air purification photocatalyst.* Journal of Alloys and Compounds, 2019. **797**: p. 166-173.

33.   Jayashree, M., M. Parthibavarman, and S. Prabhakaran, *Hydrothermal-induced"Q-Fe2O3/graphene nanocomposite with ultrahigh capacitance for stabilized and enhanced supercapacitor electrodes.* Ionics, 2019. **25**: p. 3309-3319.

34.   Devi, H.F. and T.D. Singh, *Optical properties of porous Sm3+-doped yttrium orthophosphate nanoparticles tailored by co-precipitation route.* Optics Communications, 2019. **439**: p. 34-37.

35.   Gao, S., et al., *effect of different Co contents on the microstructure and tensile strength of Mg-Co-Y alloys.* Materials Science and Engineering: A, 2019. **750**: p. 91-97.

36.   Miyawaki, R., J. Kuriyama, and I. Nakai, *The redefinition of tengerite-(Y), Y2(CO3)3·2-3H2O, and its crystal structure.* American Mineralogist, 1993. **78**(3-4): p. 425-432.

37.   Ribeiro, C., et al., *Electroactive poly(vinylidene fluoride)-based structures for advanced applications.* Nature Protocols, 2018. **13**(4): p. 681-704.

38.   Janusz, W., et al., *Synthesis and thermogravimetric analysis of monoclinic yttrium citrate dihydrate.* Journal of Thermal Analysis and Calorimetry, 2020.

39.   Lori, N., et al., *Magnetic Nanoparticles in Medical Diagnostic Applications: Synthesis, Characterization and Proteins Conjugation.* Current Nanoscience, 2016. **12**(4): p. 455-468.

40.   Serra, J.P., et al., *Ionic liquid based Fluoropolymer solid electrolytes for Lithium-ion batteries.* Sustainable Materials and Technologies, 2020. **25**: p. e00176.

41.   Komorowicz, I. and D. Barałkiewicz, *Determination of total arsenic and arsenic species in drinking water, surface water, wastewater, and snow from Wielkopolska, Kujawy-Pomerania, and Lower Silesia provinces, Poland.* Environmental Monitoring and Assessment, 2016. **188**(9): p. 504.

42.   Dummer, T.J., et al., *Geostatistical modelling of arsenic in drinking water wells and related toenail arsenic concentrations across Nova Scotia, Canada.* Sci Total Environ, 2015. **505**: p. 1248-58.

43.   Tara, N., et al., *Reduce graphene oxide-manganese oxide-black cumin based hybrid composite (rGO-MnO2/BC): A novel material for water remediation.* Materials Today Communications, 2020. **25**.

44.   Altowayti, W.A.H., et al., *The adsorptive removal of As (III) using biomass of arsenic resistant Bacillus thuringiensis strain WS3: Characteristics and modelling studies.* Ecotoxicology and Environmental Safety, 2019. **172**: p. 176-185.

45.   Choong, C.E., et al., *Granular Mg-Fe layered double hydroxide prepared using dual polymers: Insights into synergistic removal of As(III) and As(V).* Journal of Hazardous Materials, 2021. **403**.

46.   Zhang, T., et al., *Amorphous Fe/Mn bimetal–organic frameworks: outer and inner structural designs for efficient arsenic(iii) removal.* Journal of Materials Chemistry A, 2019. **7**(6): p. 2845-2854.

47.   Sherlala, A.I.A., et al., *Adsorption of arsenic using chitosan magnetic graphene oxide nanocomposite.* Journal of Environmental Management, 2019. **246**: p. 547-556.

48.   Yu, Y., et al., *An innovative yttrium nanoparticles/PVA modified PSF membrane aiming at decontamination of arsenate.* Journal of Colloid and Interface Science, 2018. **530**: p. 658-666.

49.   Guo, J., et al., *Synthesis of a novel ternary HA/Fe-Mn oxides-loaded biochar composite and its application in cadmium(II) and arsenic(V) adsorption.* Journal of Environmental Sciences, 2019. **85**: p. 168-176.

50.   Lu, J., et al., *New insights on nanostructure of ordered mesoporous FeMn bimetal oxides (OMFMs) by a novel inverse micelle method and their superior arsenic sequestration performance: Effect of calcination temperature and role of Fe/Mn oxides.* Science of The Total Environment, 2021. **762**: p. 143163.

51.   Zeng, H., et al., *As(V) adsorption by a novel core-shell magnetic nanoparticles prepared with Iron-containing water treatment residuals.* Science of The Total Environment, 2021. **753**: p. 142002.

52.   Huang, Z., et al., *Selective removal of high concentration arsenate from aqueous solution by magnetic Fe–Y binary oxide.* Colloids and Surfaces A: Physicochemical and Engineering Aspects, 2020. **603**: p. 125242.

53.   Liu, B., et al., *As(III) removal from aqueous solution using α-Fe2O3 impregnated chitosan beads with As(III) as imprinted ions.* Desalination, 2011. **272**(1): p. 286-292.

54.   Buamah, R., B. Petrusevski, and J.C. Schippers, *Presence of arsenic, iron and manganese in groundwater within the gold-belt zone of Ghana.* Journal of Water Supply: Research and Technology-Aqua, 2008. **57**(7): p. 519-529.

55.   Nguyen, K.P. and R. Itoi, *Source and release mechanism of arsenic in aquifers of the Mekong Delta, Vietnam.* Journal of Contaminant Hydrology, 2009. **103**(1): p. 58-69.

56.   Vivona, R., et al., *Occurrence of minor toxic elements in volcanic-sedimentary aquifers: a case study in central Italy.* Hydrogeology Journal, 2007. **15**(6): p. 1183-1196.

57.   Chen, C., et al., *Efficient degradation of roxarsone and simultaneous in-situ adsorption of secondary inorganic arsenic by a combination of Co3O4-Y2O3 and peroxymonosulfate.* Journal of Hazardous Materials, 2021. **407**: p. 124559.

58.   He, J., et al., *New insight into adsorption and co-adsorption of arsenic and tetracycline using a Y-immobilized graphene oxide-alginate hydrogel: Adsorption behaviours and mechanisms.* Science of The Total Environment, 2020. **701**: p. 134363.

59.   Li, Z., et al., *Efficient capture of arsenate from alkaline smelting wastewater by acetate modulated yttrium based metal-organic frameworks.* Chemical Engineering Journal, 2020. **397**: p. 125292.

60.   Chen, C., et al., *Mechanism of Arsenate Adsorption by Basic Yttrium Carbonate in a Fixed-Bed Column.* Environmental Engineering Science, 2017. **34**(11): p. 785-791.

61.   Devi, R.R., et al., *Removal of iron and arsenic (III) from drinking water using iron oxide-coated sand and limestone.* Applied Water Science, 2014. **4**(2): p. 175-182.

62.   Cao, C.Y., et al., *Low-cost synthesis of flowerlike α-Fe$_2$O$_3$ nanostructures for heavy metal ion removal: Adsorption property and mechanism.* Langmuir, 2012. **28**(9): p. 4573-4579.

63.   Karimi, P., et al., *Arsenic Removal from Mining Effluents Using Plant-Mediated, Green-Synthesized Iron Nanoparticles.* Processes, 2019. **7**(10).

64.   Huo, L., et al., *Enhanced removal of As (V) from aqueous solution using modified hydrous ferric oxide nanoparticles.* Scientific Reports, 2017. **7**(1): p. 40765.